The Astrophysical Journal, 906:12 (13pp), 2021 January 1 https://doi.org/10.3847/1538-4357/abc554

A Closer Look at Two of the Most Luminous Quasars in the Universe

Jan-Torge Schindler[1], Xiaohui Fan[2], Mladen Novak[1], Bram Venemans[1], Fabian Walter[1], Feige Wang[2,3], Jinyi Yang[2], Minghao Yue[2], Eduardo Bañados[1], and Yun-Hsin Huang[2]
[1] Max Planck Institut für Astronomie, Königstuhl 17, D-69117, Heidelberg, Germany; schindler@mpia.de
[2] Steward Observatory, University of Arizona, 933 North Cherry Avenue, Tucson, AZ 85721, USA
Received 2020 August 28; revised 2020 October 20; accepted 2020 October 26; published 2020 December 29

Abstract

Ultraluminous quasars ($M_{1450} \leqslant -29$) provide us with a rare view into the nature of the most massive and most rapidly accreting supermassive black holes (SMBHs). Following the discovery of two of these extreme sources, J0341+1720 ($M_{1450} = -29.56$, $z = 3.71$) and J2125−1719 ($M_{1450} = -29.39$, $z = 3.90$), in the Extremely Luminous Quasar Survey (ELQS) and its extension to the Pan-STARRS 1 footprint (PS-ELQS), we herein present an analysis of their rest-frame UV to optical spectroscopy. Both quasars harbor very massive SMBHs with $M_{\rm BH} = 6.73^{+0.75}_{-0.83} \times 10^9\,M_\odot$ and $M_{\rm BH} = 5.45^{+0.60}_{-0.55} \times 10^9\,M_\odot$, respectively, showing evidence of accretion above the Eddington limit ($L_{\rm bol}/L_{\rm Edd} = 2.74^{+0.39}_{-0.27}$ and $L_{\rm bol}/L_{\rm Edd} = 3.01^{+0.34}_{-0.30}$). NOEMA 3 millimeter observations of J0341+1720 reveal a highly star-forming (SFR $\approx 1500\,M_\odot\,{\rm yr}^{-1}$), ultraluminous infrared galaxy ($L_{\rm IR} \approx 1.0 \times 10^{13}\,L_\odot$) host, which, based on an estimate of its dynamical mass, is only ∼30 times more massive than the SMBH it harbors at its center. As examples of luminous super-Eddington accretion, these two quasars provide support for theories that explain the existence of billion solar mass SMBHs ∼700 million years after the Big Bang by moderate super-Eddington growth from standard SMBH seeds.

Unified Astronomy Thesaurus concepts: Supermassive black holes (1663); Quasars (1319); Astrophysical black holes (98); Active galactic nuclei (16); AGN host galaxies (2017); Millimeter astronomy (1061); Spectroscopy (1558); Active galaxies (17); Ultraluminous infrared galaxies (1735)

1. Introduction

Ultraluminous quasars host the most massive and/or the most rapidly accreting SMBHs making them prime targets in the search for supermassive black holes (SMBHs) accreting above the Eddington limit. Additionally, their analysis offers insight into a range of science questions, often related to BH formation and evolution. (i) Their discovery places strong constraints on the bright end of the quasar luminosity function (Schindler et al. 2019b). (ii) The bright background emission of ultraluminous quasars facilitates studies of the metal-enrichment in the intervening intergalactic medium (Simcoe et al. 2004) and foreground galaxies (Ryan-Weber et al. 2009; Simcoe et al. 2011). (iii) Their BH mass estimates provide important constraints on the proposed maximum-mass limit (Inayoshi & Haiman 2016; King 2016) of SMBHs, on SMBH seeds, and early BH mass growth. (iv) They allow us to probe the relation between SMBHs and the formation of the most massive galaxies.

In part driven by recent efforts to find extremely luminous quasars in the southern hemisphere (Calderone et al. 2019; Schindler et al. 2019a; Boutsia et al. 2020; Wolf et al. 2020), past years have seen the discovery of several ultraluminous sources (Wang et al. 2015; Wu et al. 2015; Wolf et al. 2018; Schindler et al. 2019b, 2019a; Jeram et al. 2020) at $z \approx 2.5$–6.5. In this paper we present follow-up observations on two of them. J0341+1720 was discovered as part of the Extremely Luminous Quasar Survey (ELQS; Schindler et al. 2017) and published in Schindler et al. (2019b) with a redshift of $z = 3.69$ determined from the optical discovery spectrum. J2125−1719 was later discovered during an extension of the ELQS to the Panoramic Survey Telescope and Rapid Response System (Pan-STARRS 1, Kaiser et al. 2002, 2010) 3π survey (PS1; Chambers et al. 2016) footprint (PS-ELQS; Schindler et al. 2019a) with a discovery redshift of $z = 3.90$. Table 1 provides an overview over the general properties of both quasars, their redshifts, absolute magnitudes at a rest-frame wavelength of 1450 Å, coordinates, and discovery photometry. J0341+1720 and J2125−1719 are ultraluminous quasars with $M_{1450} = -29.46$ and -29.35, respectively, as derived from their *i*-band magnitudes (see Figure 1). In this paper we report on the results from follow-up campaigns providing a much more detailed look into the nature of these two systems.

We present the near-infrared and optical spectroscopy of J0341+1720 and J2125−1719 in Section 2, including the model fitting, analysis and results. Section 3 describes the NOEMA 3 mm observations of J0341+1720 and their analysis. In Section 4 we discuss the possibility of these quasars being lensed, evidence for accretion beyond the Eddington limit, and put the observations of J0341+1720 in context with SMBH galaxy coevolution. A brief summary is given in Section 5. We report all magnitudes in the AB photometric system, unless otherwise noted. For cosmological calculations we have adopted a standard flat ΛCDM cosmology with $H_0 = 70\,{\rm km\,s^{-1}\,Mpc^{-1}}$, $\Omega_{\rm M} = 0.3$, and $\Omega_\Lambda = 0.7$.

2. Optical and Near-infrared Spectroscopy

2.1. J0341+1720 Observations

The two optical spectra of J0341+1720 were taken on 2016 December 19 using the VATTSpec spectrograph on the Vatican Advanced Technology Telescope (VATT). We used the 300 g mm^{-1} grating in first order blazed at 5000 Å. The spectra have a resolution of $R \sim 1000$ (1.″5 slit) and a coverage of ∼4000 Å around our chosen central wavelength of ∼5775 Å. Each spectrum was exposed for 900 s. Observations

[3] Hubble Fellow.

Table 1
General Properties of the Two Quasars

Property	J0341+1720	J2125−1719
Discovery reference	ELQS	PS-ELQS
Discovery redshift	3.69	3.90
M_{1450} (mag, *i*-band)[a]	−29.46	−29.35
Redshift (this work)	3.7078 ± 0.0005	3.9011 ± 0.0003
Redshift method	CO(4–3)	O[III]5007 Å
——— Optical survey ———		
Survey	SDSS	PS1
R.A. (deg)	55.46319	321.42069
$\sigma_{\mathrm{R.A.}}$ (deg)	0.00180	0.00533
Decl. (deg)	17.34715	−17.33095
$\sigma_{\mathrm{Decl.}}$ (deg)	0.00184	0.00327
u-band (mag)	23.036 ± 0.779	…
g-band (mag)	17.394 ± 0.014	17.710 ± 0.007
r-band (mag)	16.383 ± 0.020	16.504 ± 0.008
i-band (mag)	16.193 ± 0.014	16.422 ± 0.003
z-band (mag)	16.085 ± 0.014	16.419 ± 0.008
y-band (mag)	…	16.287 ± 0.010
——— 2MASS ———		
J-band (mag)	15.94 ± 0.05	16.13 ± 0.6
H-band (mag)	15.82 ± 0.05	16.14 ± 0.07
K-band (mag)	15.62 ± 0.06	16.01 ± 0.07
———AllWISE ———		
W1 (mag)	15.61 ± 0.02	15.92 ± 0.03
W2 (mag)	15.66 ± 0.02	16.31 ± 0.03
W3 (mag)	14.10 ± 0.03	15.56 ± 0.09
W4 (mag)	13.34 ± 0.08	14.96 ± 0.33
——— Gaia ———		
R.A. (deg)	55.46321	321.42069
$\sigma_{\mathrm{R.A.}}$ (mas)	0.07402	0.09780
Decl. (deg)	17.34716	−17.33095
$\sigma_{\mathrm{Decl.}}$ (mas)	0.05345	0.08838
G (mag)[b]	16.71	16.87
BP (mag)[b]	17.37	17.46
RP (mag)[b]	15.95	16.16

Notes.
[a] We include the values for M_{1450} (mag, *i*-band) here for comparison with quasars in Figure 1. In Table 2 we provide the updated values derived from the spectral fits.
[b] Gaia magnitudes are in the Vega system. The Gaia DR2 does not provide an error for this quantity as the error distribution is only symmetric in flux space.

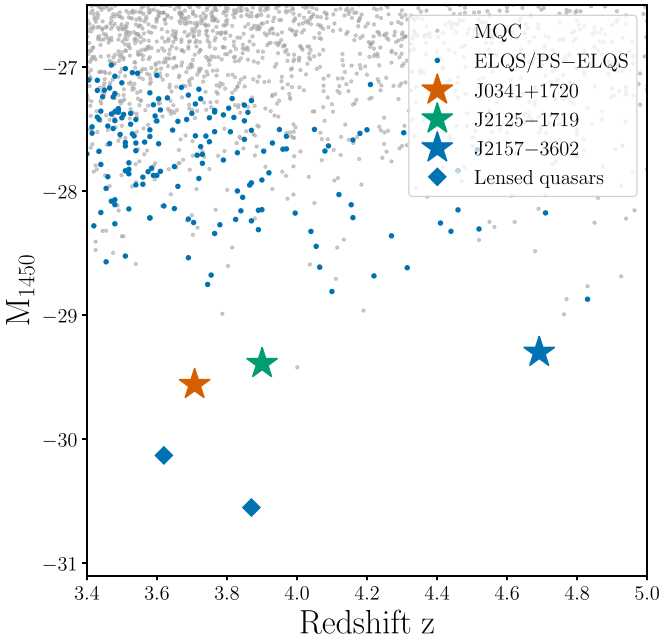

Figure 1. Quasars in the plane of absolute magnitude at 1450 Å, M_{1450}, and redshift, *z*. We highlight the two quasars of this study, J0341+1720 and J2125-1710, as orange and green stars, respectively. We further display J2157-3602, an ultraluminous quasar at $z = 4.692$ (Wolf et al. 2018; Onken et al. 2020) as the blue star and two prominent lensed quasars as blue diamonds. Gray dots in the background show the quasar distribution based on the Million Quasar Catalogue (MQC; Flesch 2015, v5.7b). We calculate the absolute magnitude, M_{1450}, for all sources based on the PS1 *i*-band photometry as in Schindler et al. (2019a). Quasars discovered as part of the ELQS and PS-ELQS surveys are highlighted in blue.

are carried out with the slit aligned with the parallactic angle to minimize slit losses.

We reduced the optical spectra using the standard long slit reduction routines within the IRAF software (Tody 1986, 1993). One-dimensional spectra were extracted with the apall routine using the built-in cosmic-ray removal and optimal extraction (Horne 1986). We calibrated the wavelength using the internal VATTSpec HgAr lamp. Relative flux calibration was done using a standard flux calibrator. The spectra have not been corrected for telluric absorption.

The near-infrared follow-up spectroscopy was taken on 2018 November 24 using the LUCI 1 and LUCI 2 instruments in binocular mode on the Large Binocular Telescope (LBT). We used the G200, 200 g mm^{-1} grating, on LUCI 1 in the HKspec filter band covering the wavelength range of 13200–24000 Å with a resolution of $R \approx 630$–870 (1.″5 slit). The simultaneously executed observations with LUCI 2 used the G200, 200 g mm^{-1} grating, in the zJspec filter band covering a wavelength range of 9000–12500 Å with a resolution of $R \approx 700$–800 (1.″5 slit). Four exposures of 150 s each were taken in a standard ABBA dithering pattern.

The near-infrared spectra were reduced with the open source "Python Spectroscopic Data Reduction Pipeline," `PypeIt`[4] (Prochaska et al. 2019, 2020). The pipeline automatically traces the long-slit spectra and corrects for detector illumination. Skylines are subtracted by difference imaging on the dithered AB pairs and with a 2D BSpline fitting procedure. The 1D spectra are extracted using the optimal spectrum extraction technique (Horne 1986) along automatically identified traces. Relative flux calibration is done using the standard star HD 24000 observed during the same night. The four individual exposures are then coadded and corrected for telluric absorption. The pipeline uses a large grid of telluric models produced from the Line-By-Line Radiative Transfer Model (LBLRTM4; Clough et al. 2005; Gullikson et al. 2014) to find the best-fit model, which corrects the absorbed quasar spectrum up to a best-fit PCA model (Davies et al. 2018) of it.

Due to the changing and nonoptimal weather conditions absolute flux calibration using the standard stars is not reliable. After coadding the optical spectra we have flux calibrated them using the SDSS *r*-band magnitude of the quasar. The zJband and HKband spectra were similarly flux calibrated using the *J*-band and *K*-band photometry of 2MASS. All spectra have been extinction corrected[5] using the extinction law of Fitzpatrick &

[4] https://github.com/pypeit/PypeIt
[5] We used the python package `extinction` (Barbary 2016) to calculate the extinction correction.

Massa (2007) with $R_V = 3.1$ and $A_V = 0.45$ (Schlafly & Finkbeiner 2011).

2.2. J2125−1719 Observations

The optical discovery spectra of J2125−1719 were taken on 2017 October 7 and 10 with the Goodman High Throughput Spectrograph (Goodman HTS) on the Southern Astrophysical Research (SOAR) Telescope (4.1 m). Observations using the 400 g mm^{-1} grating with central wavelengths of 6000 and 7300 Å resulted in spectra with a wavelength coverage of ∼4000–8000 Å (GG-385 blocking filter) and ∼5300–9300 Å (GG-495 blocking filter), respectively. All observations used the red camera in 2 × 2 spectral binning mode. The ∼4000–8000 Å "blue" spectrum was observed for 600 s with the 1.″2 slit resulting in a resolution of $R \approx 690$. For the ∼5300–9300 Å "red" spectrum we exposed for 900 s using the 1.″0 slit, which provides a slightly better resolution of $R \approx 830$. The spectra were reduced with IRAF using the same methods as for the optical spectra in Section 2.1.

The near-infrared follow-up spectroscopy was carried out with the Folded-port InfraRed Echellete spectrograph (FIRE; Simcoe et al. 2013) at Magellan Baade. We have taken a FIRE Echelle spectrum using the 0.″75 slit over the nominal spectral range of ∼8250–25200 Å with a resolution of $R \approx 6000$ on 2018 September 25. The near-infrared FIRE spectrum was also reduced using *PypeIt* as described for J0341+1720 in Section 2.1. The optical and near-infrared spectra were also extinction corrected using the extinction law of Fitzpatrick & Massa (2007) with $R_V = 3.1$ and $A_V = 0.16$ (Schlafly & Finkbeiner 2011).

To generate the composite spectrum the near-infrared spectrum was flux calibrated to the 2MASS *K*-band magnitude. We scaled the "red" SOAR spectrum to the near-infrared spectrum in the region of 8500–9000 Å and joined them at 8500 Å. We further added the "blue" SOAR spectrum to the composite blueward of 6500 Å, scaling the "blue" SOAR spectrum flux to match the composite in the 6000–7000 Å overlap region.

2.3. Modeling of the Optical and Near-infrared Spectroscopy

A general description of our fitting procedure, detailing the continuum models, line models, and basic wavelength regions included in the fit, is given in the Appendix. Figures 2 and 3 show the full composite spectra and their best-fit model (solid orange line) for J0341+1720 and J2125−1719, respectively. The bottom panel in each figure shows the full wavelength coverage, whereas the top panels provide a detailed view on the emission lines of interest. We masked out regions severely affected by telluric absorption or reduction artifacts at the edges. This reduces the nominal coverage of the LUCI 1/2 spectra of J0341+1720 in Figure 2. In the following we describe details on the spectral modeling specific to each quasar and exceeding the general description in the Appendix.

We have fit J0341+1720 twice using both the Tsuzuki et al. (2006) and the Vestergaard & Wilkes (2001) iron templates. The only property we adopt from the fit with the Vestergaard & Wilkes (2001) template is the FWHM of Mg II to estimate the Mg II-based black hole mass using the Vestergaard & Osmer (2009) relation. To model the composite spectrum of J0341+1720 we approximate each of the Si IV+O IV], C IV and Mg II lines with one Gaussian component. To accurately describe the Hβ line we use two Gaussian components. The Si IV line appears to be broad and significantly blueshifted. We thus reduce the blueward $\lambda_{\rm rest} = 1340$–$1375$ Å continuum window, to fit the line in a larger rest-frame wavelength window of $\lambda_{\rm rest} = 1350$–$1425$ Å. For the C IV, Mg II, and the Hβ and [O III] lines we use the wavelength ranges of $\lambda_{\rm rest} = 1480$–$1600$ Å, $\lambda_{\rm rest} = 2740$–$2860$ Å, and $\lambda_{\rm rest} = 4700$–$5050$ Å, respectively. We interactively mask out regions affected by strong absorption features, leading to the emission line windows as seen in Figure 2 (light orange bars).

In the case of J2125−1719 we only incorporate the iron template of Boroson & Green (1992) as we do not fit the Mg II region. One Gaussian component is used to approximate the Si IV+O IV], [O III] λ4960 Å, and [O III] λ5007 Å emission lines, while we use two Gaussian components for the C IV and Hβ lines. We fit the Si IV+O IV], C IV, and the Hβ and [O III] emission lines in the wavelength ranges of $\lambda_{\rm rest} = 1375$–$1425$ Å, $\lambda_{\rm rest} = 1500$–$1600$ Å, and $\lambda_{\rm rest} = 4700$–$5050$ Å, respectively. We have masked out the wavelength region of $\lambda = 7586$–7679 Å from the C IV emission line fit as it is strongly affected by telluric absorption features not corrected in the reduction process. In addition, we mask out regions affected by narrow absorption lines as well as residuals from strong sky lines (see Figure 3).

2.4. Results of the Optical and Near-infrared Spectroscopy

Tables 2 and 3 summarize the measurements of the continuum and line properties from our fit analysis. The tables provide the median with the associated 13.6 and 86.4 percentile uncertainties of our resampled posterior distribution (see the Appendix).

We would like to caution the reader that these results can be sensitive to assumptions made when modeling the spectra, such as the choice of the continuum windows. In the case of high signal-to-noise ratio data, the impact of these assumptions can be larger than the statistical uncertainties from the fitting. Therefore, we have been fully transparent about all assumptions we made, as detailed in Section 2.3 and the Appendix.

Our models provide a global fit to the full wavelength range of both spectra. In these cases the continuum fit can over- or underestimate specific regions of the spectrum. As an example, we quantify differences in the continuum properties by directly measuring the absolute magnitude at 1450 Å from the spectrum. We measure $M_{1450} = -29.529 \pm 0.043$ and $M_{1450} = -29.422 \pm 0.012$ for J0341+1720 and J2125−1719, respectively, showing differences of $|\Delta M_{1450}| = 0.04$ to the fit measurements, about a factor of ∼10 larger than the pure statistical uncertainties given in Table 2.

Line redshifts are measured from the peak flux wavelength of the full emission line models. This means that line models made from multiple components are summed before the peak flux wavelength is determined. We derive velocity shifts from the line redshifts with respect to the systemic quasar redshift using *linetools* (Prochaska et al. 2016) including relativistic corrections. For J0341+1720 we adopt the CO(4–3) line redshift, $z = 3.7078$ (see Section 3), as the systemic redshift for J0341+1720. In the case of J2125−1719 the redshift of the [O III]$_{5007\ \text{Å}}$ line serves as our best estimate for its systemic redshift.

For each line we calculate the FWHM, equivalent width (EW), integrated flux, and integrated luminosity from the full line model, including all Gaussian components. The spectral

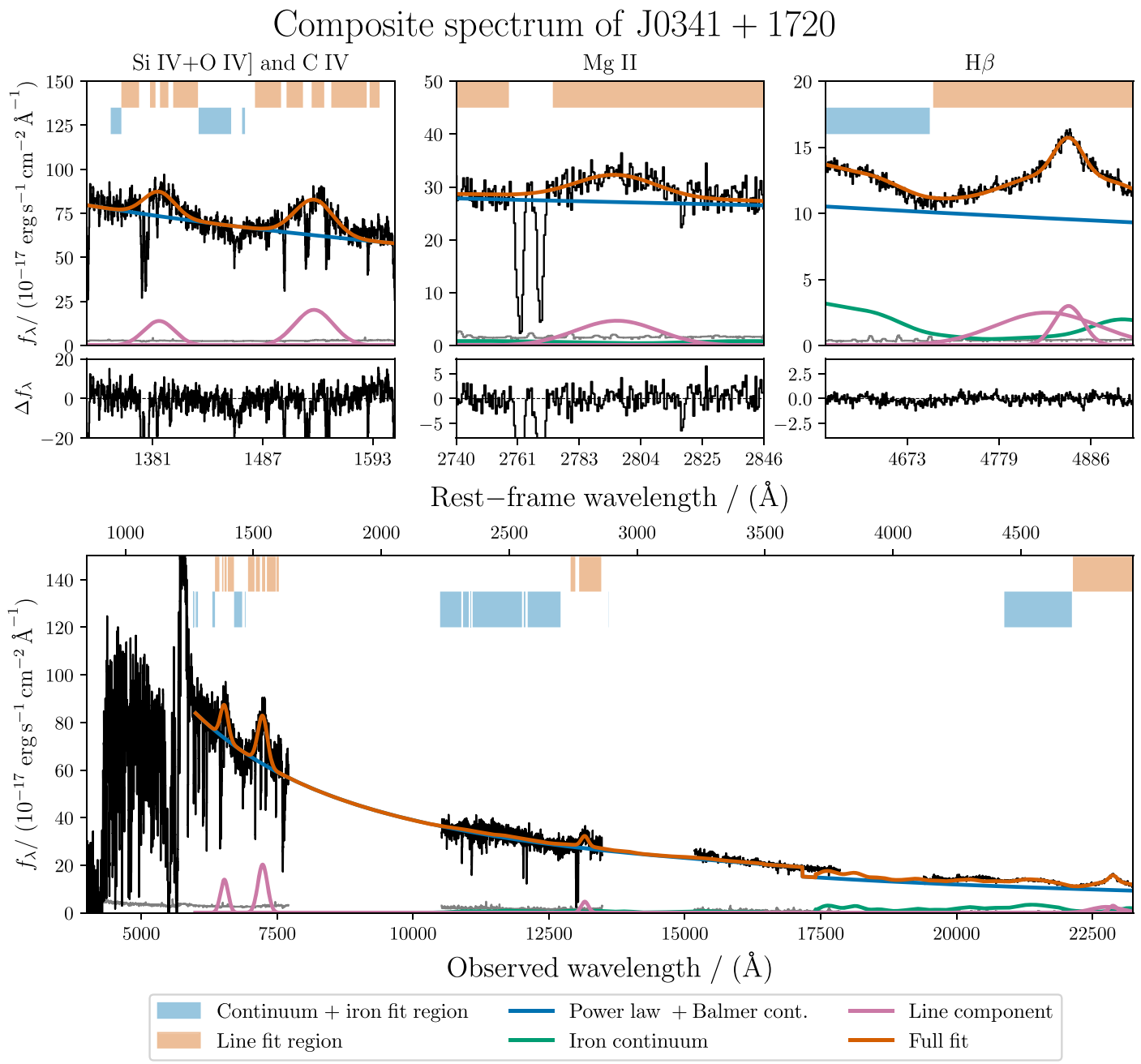

Figure 2. Optical to near-infrared composite spectrum of J0341+1720 including the best-fit model from our analysis. The lower panel shows the full composite spectrum, while the upper panels display the emission line fits around the Si IV+O IV] and C IV, Mg II, and Hβ lines in more detail. The best-fit model is highlighted as the solid orange line. Solid blue, green, and pink lines show the individual power law and Balmer continuum, iron continuum, and line component models. Flux uncertainties are given by the gray line. Light blue and orange bars at the top of each panel highlight which wavelength regions were included in the continuum (power law + Balmer continuum & iron FeII continuum) and emission line fits. The presented best-fit model uses the Tsuzuki et al. (2006) iron template in the Mg II region and the Boroson & Green (1992) iron template around Hβ.

resolution (R) can broaden the lines and therefore we correct each line FWHM by:

$$\mathrm{FWHM} = \sqrt{\mathrm{FWHM}^2_{\mathrm{obs}} - \mathrm{FWHM}^2_{\mathrm{R}}}. \quad (1)$$

In the case of J0341+1720 we determine the integrated flux and the luminosity of the Fe II pseudo-continuum in the wavelength range of 2200–3090 Å, to construct the Fe II/Mg II flux ratio, a measure for BLR iron enrichment in high-redshift quasars (Dietrich et al. 2003). This wavelength region was chosen to be comparable with other studies in the literature (e.g., Dietrich et al. 2003; Maiolino et al. 2003; Kurk et al. 2007; De Rosa et al. 2011; Mazzucchelli et al. 2017). We calculate a value of $F_{\mathrm{Fe\,II}}/F_{\mathrm{Mg\,II}} = 2.78^{+0.79}_{-0.65}$, which is on the lower end of the distribution compared to quasars at $z > 3$ (for a comparison, see Onoue et al. 2020, their Figure 5, filled symbols). The inset of the Mg II line in Figure 2 highlights the small iron contribution around Mg II. The iron flux around the Hβ line is much stronger, highlighting how the iron contribution can vary throughout the spectrum.

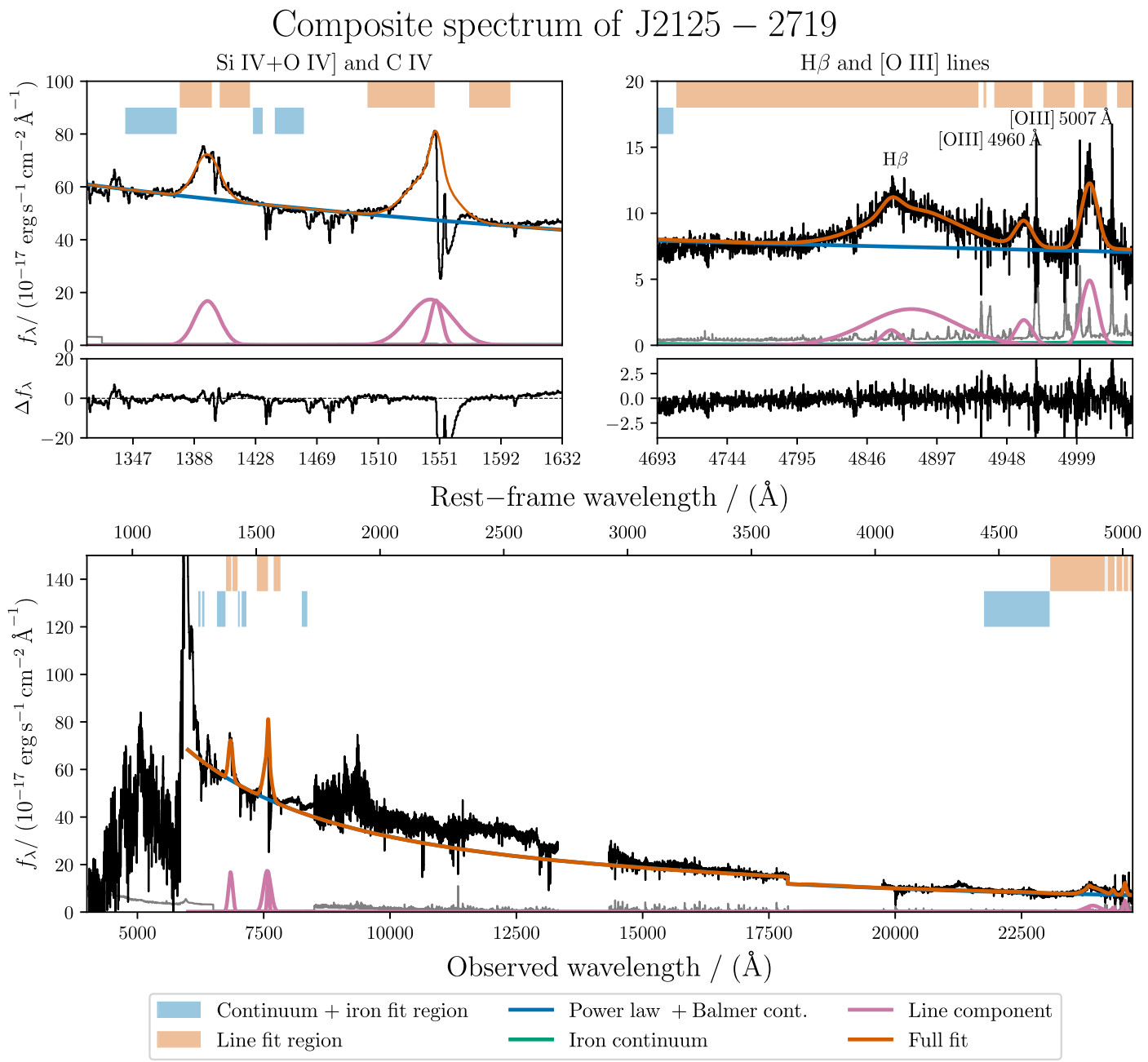

Figure 3. Optical to near-infrared composite spectrum of J2125−1719 including the best-fit model from our analysis. The lower panel shows the full composite spectrum, while the upper panels display the emission line fits of Si IV and C IV and Hβ and [O III] in more detail. For the description of the lines and symbols, see Figure 2.

2.4.1. Bolometric Luminosity, Black Hole Mass, and Eddington Luminosity Ratio

The spectral properties measured from the model fits allow us to derive the bolometric luminosity, the black hole mass, and the Eddington luminosity ratio. We calculate the bolometric luminosity following Shen et al. (2011):

$$L_{\rm bol} = 5.15 \cdot \lambda L_{\lambda,3000}. \quad (2)$$

We estimate black hole masses assuming that the line-emitting gas of the Mg II and Hβ lines is in virial motion around the SMBH. Then the line-of-sight velocity dispersion traces the gravitational potential of the SMBH mass ($M_{\rm BH}$). Based on reverberation mapping results (e.g., Onken et al. 2004; Peterson et al. 2004), single-epoch virial estimators (e.g., Vestergaard & Peterson 2006; Vestergaard & Osmer 2009) allow us to infer the SMBH mass by measuring the FWHM of broad quasar emission lines and their continuum luminosities. However, these measurements have large systematic uncertainties of ∼0.4–0.55 dex (Vestergaard & Osmer 2009; Shen 2013). Single-epoch virial estimators are often written as

$$M_{\rm BH} = 10^{zp(x)} \cdot \left[\frac{\rm FWHM}{1000\ {\rm km\ s^{-1}}}\right]^2 \left[\frac{xL_{\lambda,x}}{10^{44}\ {\rm erg\ s^{-1}}}\right]^b M_\odot, \quad (3)$$

where zp, the zero-point BH mass, and the slope b depend on the chosen emission line and continuum luminosity. We derive black hole masses based on the Mg II, Hβ, and C IV line. Using

Table 2
Quasar Properties Directly Measured or Derived from the Spectral Fits

Measured Property	J0341+1720	J2125−1719
M_{1450}/(mag)	$-29.562^{-0.004}_{+0.004}$	$-29.386^{-0.001}_{+0.001}$
$L_{3000}/(10^{46}$ erg s$^{-1})$	$44.96^{+0.22}_{-0.21}$	$40.13^{+0.11}_{-0.10}$
$L_{3000,\mathrm{VW01}}/(10^{46}$ erg s$^{-1})$	$44.98^{+0.20}_{-0.21}$	…
$L_{5100}/(10^{46}$ erg s$^{-1})$	$27.22^{+0.25}_{-0.25}$	$25.26^{+0.14}_{-0.13}$
Power-law index α	$-1.620^{+0.007}_{-0.008}$	$-1.551^{+0.004}_{-0.004}$
$F_{\mathrm{Fe\ II}}/F_{\mathrm{Mg\ II}}$	$2.78^{+0.79}_{-0.65}$	…
Derived property	**J0341+1720**	**J2125-1719**
$L_{\mathrm{bol}}/(10^{48}$ erg s$^{-1})$	$2.32^{+0.01}_{-0.01}$	$2.07^{+0.01}_{-0.01}$
Mg II BH mass (VW09)/$(10^9\,M_\odot)$	$7.47^{+1.63}_{-1.35}$	…
$\lambda_{\mathrm{Edd,MgII}}$ (VW09)	$2.47^{-0.44}_{+0.54}$	…
Hβ BH mass (VO06) $(10^9\,M_\odot)$	$6.73^{+0.75}_{-0.83}$	$5.45^{+0.60}_{-0.55}$
$\lambda_{\mathrm{Edd,H}\beta}$ (VO06)	$2.74^{-0.27}_{+0.39}$	$3.01^{-0.30}_{+0.34}$
C IV BH mass (VO06) $(10^9\,M_\odot)$	$33.80^{+2.11}_{-2.43}$	$4.53^{+0.36}_{-0.38}$
$\lambda_{\mathrm{Edd,C\ IV}}$ (VO06)	$0.55^{-0.03}_{+0.04}$	$3.63^{-0.27}_{+0.33}$
C IV BH mass (Co17) $(10^9\,M_\odot)$	$14.20^{+1.22}_{-1.16}$	…
$\lambda_{\mathrm{Edd,C\ IV}}$ (Co17)	$1.30^{+0.12}_{-0.10}$	…

Note. All properties of J0341+1720 are from the fit with the Tsuzuki et al. (2006) iron template with the exception of $L_{3000,\mathrm{VW01}}$, for which the Vestergaard & Wilkes (2001) iron template was used.
References. VW01: Iron template of Vestergaard & Wilkes (2001); VW09: BH mass estimator of Vestergaard & Osmer (2009); VO06: BH mass estimator of Vestergaard & Peterson (2006); Co17: BH mass estimator of Coatman et al. (2017).

the Mg II line we estimate SMBH masses using the single-epoch virial estimators of Vestergaard & Osmer (2009, $zp = 6.86$, $b = 0.5$, $x = 3000$ Å). For the Hβ line we adopt the virial estimator of Vestergaard & Peterson (2006, $zp = 6.91$, $b = 0.5$, $x = 5100$ Å).

Contrary to Mg II and Hβ, the C IV line often shows asymmetric line profiles in addition to large velocity blueshifts (e.g., Richards et al. 2011). The blueshifts have been shown to correlate with the equivalent width and the FWHM of the line, resulting in biases for black hole masses derived from C IV (e.g., Shen 2013; Coatman et al. 2016; Mejía-Restrepo et al. 2018). A range of studies have thus proposed corrections for these biases (e.g., Denney 2012; Park et al. 2013; Runnoe et al. 2013; Mejía-Restrepo et al. 2016; Coatman et al. 2017), which are not always applicable to all quasars, e.g., depending on their luminosity or Eddington ratio (Mejía-Restrepo et al. 2018). Still, we decided to derive C IV-based black hole masses as well to compare them with the measurements from the Mg II and Hβ lines. We adopt Vestergaard & Peterson (2006, $zp = 6.66$, $b = 0.53$, $x = 1350$ Å) and also provide corrected BH masses according to Equations (4) and (6) of Coatman et al. (2017).

We calculate the Eddington luminosity ratio by dividing the bolometric luminosity by the Eddington luminosity:

$$\lambda_{\mathrm{Edd}} = \frac{L_{\mathrm{bol}}}{1.26 \times 10^{38}\ \mathrm{erg\ s^{-1}}} \frac{M_\odot}{M_{\mathrm{BH}}}. \quad (4)$$

As the absolute magnitude of J0341+1720 already suggests (see Figure 1), this quasar is one of the most luminous in the observable universe with a bolometric luminosity of $L_{\mathrm{bol}} = 2.32(\pm 0.01) \times 10^{48}$ erg s^{-1}. We list all black hole mass estimates and subsequent Eddington luminosity ratios in Table 2. The black hole mass estimates range from 6.73 to $33.80 \times 10^9\,M_\odot$. The large values are driven by the C IV line, which shows large C IV blueshifts. Even the correction of Coatman et al. (2017) cannot resolve the tension between the C IV and the Hβ or Mg II BH mass estimates. Therefore, we regard the C IV measurements as unreliable and only adopt the Mg II and Hβ black hole masses, $7.47 \times 10^9\,M_\odot$ and $6.73 \times 10^9\,M_\odot$, respectively. Based on these BH mass measurements we find Eddington luminosity ratios of 2.47 (Mg II) and 2.74 (Hβ), suggesting that J0341+1720 is accreting above the Eddington limit.

With a bolometric luminosity of $L_{\mathrm{bol}} = 2.07 \times 10^{48}$ erg s^{-1}, J2125−1719 is also one of the most luminous quasars at $z > 3.5$. The C IV line has only a very small blueshift and it is not necessary to apply the correction of Coatman et al. (2017) to the BH mass. The black hole mass estimates of C IV (VO06) and Hβ (VO06) show good agreement, with values of 4.53 and $5.45 \times 10^9\,M_\odot$, respectively. The subsequent Eddington luminosity ratios are $\lambda_{\mathrm{Edd,C\ IV}} = 3.63$ and $\lambda_{\mathrm{Edd,H}\beta} = 3.01$, i.e., resulting in super-Eddington accretion.

3. Millimeter Observations of J0341+1720

To determine the redshift, star formation rate, and dynamical mass of the quasar host galaxy of J0341+1720, we observed its CO(4–3) transition at rest-frame 650.3 μm ($\nu_{\mathrm{rest}} = 461.04$ GHz) using the Northern Extended Millimeter Array (NOEMA). At the redshift of the quasar, $z = 3.7078$, the CO(4–3) line shifts to 97.93 GHz or 3061.6 μm observable in Band 1 (3 mm). J0341+1720 was observed on 2019 July 1, 3, 5, and 6 with nine antennas in configuration D for a total of 9.0 hr on-source time. After applying quality cuts to the data we present results on 3.75 hr of effective on-source time. The sources J0322+222 and J0342+147 were observed every 30 minutes for phase and amplitude calibration. The absolute flux calibration was done using 3C454.3, MWC349, and LKHA101 observed at the beginning of each track. The PolyFix correlator provides a bandwidth of 7.7 GHz in each of its two sidebands for a total of 15.4 GHz. We chose a tuning frequency of 99.32 GHz to allow for simultaneous detection of the [C I] line at a rest frequency of 492.16 GHz in the upper side band in addition to the targeted CO(4–3) transition. The data was reduced and analyzed using the Grenoble Image and Line Data Analysis System (GILDAS) software.[6] We rebinned the data to a resolution of 40 MHz (≈120 km s^{-1}), resulting in an average flux (rms) uncertainty of 0.23 mJy beam^{-1}.

Figure 4 (left panel) shows the continuum map of the joint lower and upper side band, including only line-free channels. The final resolution of the image (natural weighting) is $6\farcs4 \times 4\farcs2$ at a position angle of 14°. At the source redshift 1″ corresponds to approximately 7 kpc, which means that the quasar host galaxy is unresolved in our NOEMA observations (e.g., see Venemans et al. 2020).

We fit a point source in the UV-plane to the continuum map, finding a peak flux of 0.104 mJy beam^{-1} across both side bands with a central frequency of 93.5 GHz. This results in a continuum detection with a signal-to-noise ratio of S/N > 8 ($\sigma = 11.6\ \mu$Jy beam^{-1}) . The continuum subtracted collapsed line map is displayed in Figure 4 (right panel), also displaying a significant detection. Natural weighting results in a resolution of $6\farcs1 \times 3\farcs9$ at a position angle of 14° for the CO(4–3) line.

[6] http://www.iram.fr/IRAMFR/GILDAS

Table 3
Emission Line Properties of J0341+1720 and J2125–1719

Line	$z_{\rm line,peak}$	$F_{\rm line}$ (10^{-17} erg s^{-1} cm^2)	FWHM$_{\rm line}$ (km s^{-1})	EW$_{\rm line}$ (Å)	$\Delta v(z_{\rm line}-z_{\rm sys})$ (km s^{-1})	Components
			J0341+1720			
Si IV	$3.6638^{+0.0021}_{-0.0018}$	$2459.97^{+132.59}_{-134.59}$	7588^{+311}_{-329}	$7.11^{+0.41}_{-0.41}$	-2813^{+135}_{-114}	1G
C IV	$3.6691^{+0.0013}_{-0.0013}$	$4419.30^{+127.42}_{-155.00}$	8484^{+261}_{-310}	$15.00^{+0.49}_{-0.58}$	-2473^{+85}_{-85}	1G
Mg II	$3.7024^{+0.0017}_{-0.0016}$	$783.69^{+59.00}_{-52.05}$	3551^{+362}_{-316}	$6.01^{+0.46}_{-0.40}$	-342^{+108}_{-105}	1G
Mg II (VW01)	$3.7014^{+0.0016}_{-0.0017}$	$929.43^{+68.58}_{-69.88}$	3922^{+407}_{-371}	$7.23^{+0.55}_{-0.55}$	-411^{+103}_{-111}	1G
Hβ	$3.7035^{+0.0006}_{-0.0006}$	$2274.75^{+69.02}_{-70.91}$	3983^{+215}_{-255}	$45.90^{+1.59}_{-1.65}$	-275^{+38}_{-36}	2G
CO(4–3)	3.7078 ± 0.0005	⋯	460 ± 69	⋯	0 ± 69	1G
			J2125-1719			
Si IV	$3.8886^{+0.0003}_{-0.0003}$	$1615.57^{+17.39}_{-18.85}$	4193^{+42}_{-76}	$6.28^{+0.07}_{-0.08}$	-765^{+17}_{-17}	1G
C IV	$3.8983^{+0.0026}_{-0.0019}$	$3887.95^{+177.84}_{-110.13}$	3246^{+126}_{-140}	$17.58^{+0.82}_{-0.50}$	-169^{+156}_{-117}	2G
Hβ	$3.9032^{+0.0008}_{-0.0007}$	$1176.19^{+25.84}_{-28.00}$	3653^{+197}_{-189}	$31.58^{+0.73}_{-0.85}$	131^{+47}_{-42}	2G
O[III] λ4960 Å	$3.9010^{+0.0005}_{-0.0005}$	$139.26^{+13.36}_{-12.48}$	843^{+98}_{-95}	$3.81^{+0.37}_{-0.34}$	-6^{+32}_{-29}	1G
O[III] λ5007 Å	$3.9011^{+0.0003}_{-0.0003}$	$347.49^{+17.59}_{-16.36}$	811^{+47}_{-54}	$9.58^{+0.49}_{-0.45}$	-0^{+17}_{-17}	1G

Note. All line measurements of J0341+1720 are from the fit with the Tsuzuki et al. (2006) iron template with the exception of Mg II (VW01), which was fit using the Vestergaard & Wilkes (2001) iron template.

3.1. CO(4–3) Line Fit and Estimates of the Host Galaxy's Gas Mass, Dynamical Mass, and Star Formation Rate

Figure 5 shows the spectrum in the upper side band with the CO(4–3) line clearly detected around 97.93 GHz. We have chosen a binning of 40 MHz to ensure that we detect the FWHM of the CO(4–3) at the $\sim 3\sigma$ level. At this reduced resolution instrumental effects are negligible compared to the flux uncertainties. The [C I] line is not detected, but based on the noise level we can provide a 3σ upper limit of $\sim$0.2 Jy beam^{-1} km s^{-1} choosing the same line width as for the CO(4–3) line (FWHM = 460 km s^{-1}, see below). A simple fit to the spectrum, shown as the solid orange line, approximates the spectrum with a Gaussian profile for the line and a constant flux value for the continuum. Based on our best-fit model we measure the line center at 97.9312 ± 0.0095 GHz, which corresponds to a redshift of $z_{\rm CO(4-3)} = 3.7078 \pm 0.0005$ for J0341+1720. The CO(4–3) peak line flux is 1.19 ± 0.15 mJy beam^{-1} with a line width of $\sigma_v = 63.76$ MHz. We obtain an integrated line flux of $F_{\rm CO(4-3)} = 0.58 \pm 0.12$ Jy km s^{-1} and convert it to a line luminosity following, e.g., Carilli & Walter (2013):

$$\frac{L_{\rm line}}{L_\odot} = 1.04 \cdot 10^{-3} \frac{F_{\rm line}}{\rm Jy\ km\ s^{-1}} \frac{\nu_{\rm obs}}{\rm GHz} \left(\frac{D_{\rm L}}{\rm Mpc}\right)^2, \quad (5)$$

where $\nu_{\rm obs}$ is the observed frequency of the line and $D_{\rm L}$ is the cosmological luminosity distance. We calculate a CO(4–3) line luminosity of $6.3(\pm 1.3) \times 10^7\, L_\odot$. We further evaluate the (areal) integrated source brightness temperature (also see Carilli & Walter 2013) for the CO(4–3) line:

$$\frac{L'_{\rm line}}{\rm K\ km\ s^{-1}\ pc^2} = \frac{3.25 \cdot 10^7}{(1+z)^3} \frac{F_{\rm line}}{\rm Jy\ km\ s^{-1}} \left(\frac{D_{\rm L}}{\rm Mpc} \cdot \frac{\rm GHz}{\nu_{\rm obs}}\right)^2. \quad (6)$$

The resulting CO(4–3) integrated source brightness temperature is $L'_{\rm CO(4-3)} = 2.0 \times 10^{10}$ K km s^{-1} pc^2. Based on $L'_{\rm CO(4-3)}$ and the scaling factors provided in Table 2 (QSO) of Carilli & Walter (2013) we estimate $L'_{\rm CO(1-0)} = L'_{\rm CO(4-3)}/0.87 = 2.32 \times 10^{10}$ K km s^{-1} pc^2. We use $L'_{\rm CO(1-0)}$ to estimate the gas mass of J0341+1720. Using the α conversion factor for ultraluminous infrared galaxies (ULIRG, $L_{\rm IR} \geqslant 10^{12}\, L_\odot$, see below), $\alpha_{\rm CO} \sim 0.8\, M_\odot$ (K km s^{-1} pc^2)$^{-1}$ (Downes & Solomon 1998), results in a gas mass of $M_{\rm gas} \approx 1.9 \times 10^{10}\, M_\odot$.

In the following we will derive estimates for the dynamical mass of this system. The presented observations do not resolve the host galaxy emission and we rely on mean properties of other high-redshift quasar samples for this calculation.

We measured the FWHM of the CO(4–3) line from the Gaussian fit to the spectrum, FWHM$_{\rm CO(4-3)} = 460 \pm 69$ km s^{-1} ($\sigma_v = 195 \pm 29$ km s^{-1}). Based on the FWHM measurement we continue to assess the dynamical mass of the host galaxy by using the virial theorem for the case of a dispersion dominated system:

$$M_{\rm dyn,disp} = \frac{3}{2} \frac{R_{\rm CO} \sigma_v^2}{G}, \quad (7)$$

where G is the gravitational constant and $R_{\rm CO}$ is the radius of the line-emitting region. As our millimeter observations do not spatially resolve the quasar host galaxy, we adopt a radius of $R_{\rm CO} = 2.2$ kpc for the source of the CO(4–3) emission, twice the effective (half-light) radius of [C II] emission in high-redshift quasar hosts (M. Neeleman et al. 2020, in preparation; Novak et al. 2020) with a sample uncertainty of $\sigma = 0.22$ kpc. Assuming that we can infer the gas velocity dispersion from the FWHM of the CO(4–3) we estimate a dispersion dominated dynamical mass of $M_{\rm dyn,disp} \approx 3 \times 10^{10}\, M_\odot$. If the system was rotationally supported with an inclination i, the dynamical mass can be approximated by (see Wang et al. 2013; Willott et al. 2015; Decarli et al. 2018):

$$M_{\rm dyn,rot} = \frac{R_{\rm CO}}{G} \cdot \left(\frac{3}{4} \frac{\rm FWHM}{\sin(i)}\right)^2. \quad (8)$$

For J0341+1720 we adopt an inclination of $i = 33°$, the mean inclination for quasar hosts given in M. Neeleman et al. (2020,

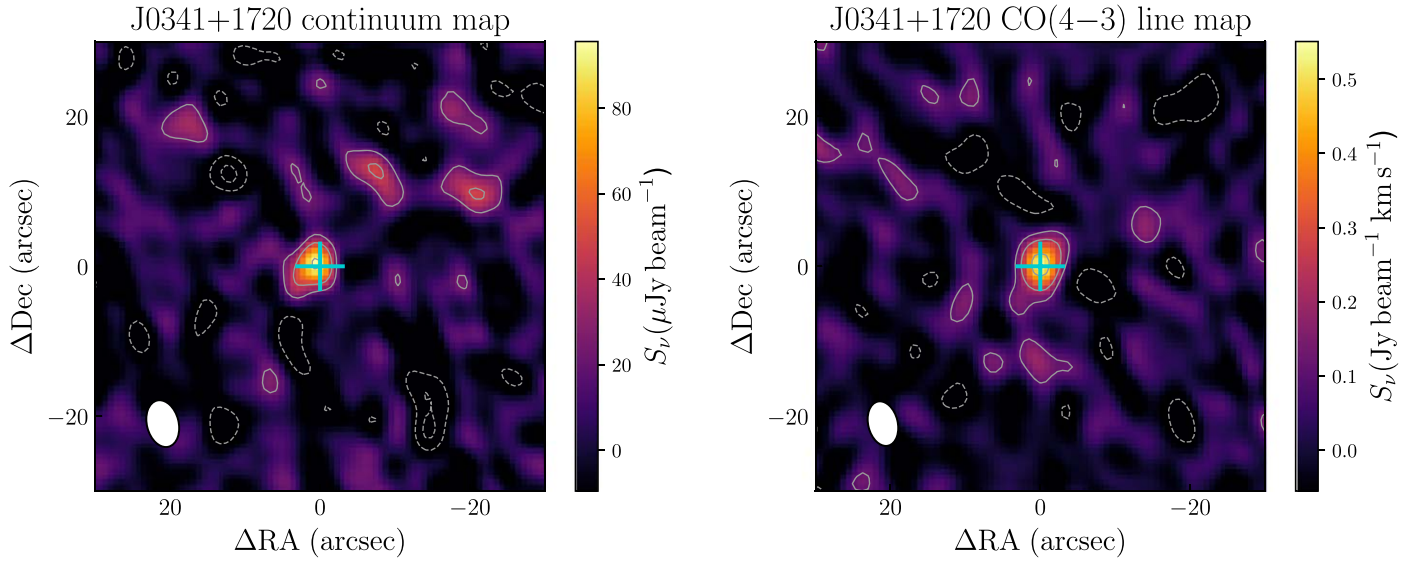

Figure 4. Intensity maps of continuum (left) and CO(4–3) line emission in J0341+1720. Solid and dashed gray contours highlight regions of positive and negative 2σ, 4σ, 8σ and the cyan cross marks the optical position of the quasar. Left: collapsed continuum emission in line-free channels across both side bands ($\sigma = 11.6\,\mu$Jy beam^{-1}). The beam FWHM of $6\farcs4 \times 4\farcs2$, shown in the left bottom corner as a white ellipse, corresponds to ∼45 kpc × 30 kpc at the redshift of the quasar. The observations do not resolve the source. Right: continuum subtracted CO(4–3) line emission of J0341+1720 averaged over $\nu = 97.6$–98.2 GHz ($\sigma = 0.06$ Jy beam^{-1} km s^{-1}). In the left bottom corner we show the beam FWHM of $6\farcs1 \times 3\farcs9$ as a white ellipse.

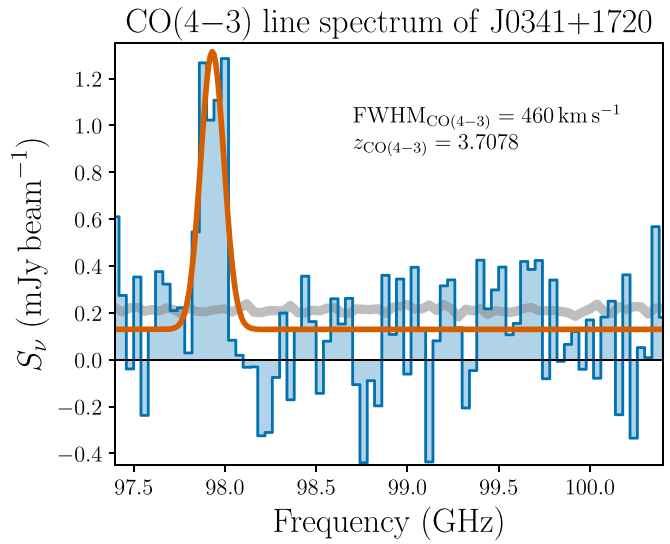

Figure 5. The upper side band spectrum of J0341+1720 at a resolution of 40 MHz (blue). The CO(4–3) line is clearly detected at $\nu = 97.93$ GHz. We display the flux (rms) uncertainty in gray and overplot the best-fit model to the spectrum (continuum + line) with the solid orange line.

in preparation). Using this assumption we infer a rotational dynamical mass of $M_{\rm dyn,rot} \approx 2 \times 10^{11}\,M_\odot$.

Lastly, we use the continuum flux to estimate the star formation rate for J0341+1720. Based on the observations in both, the lower and upper side band, we measure an average continuum flux of $S_{\rm obs,cont} = 0.104(\pm0.013)$mJy at a frequency of 93.5 GHz. This frequency probes the thermal infrared continuum of the quasar host. Assuming a modified blackbody with a dust temperature of $T_{\rm dust} = 47$ K and a power-law slope $\beta = 1.6$ (see Beelen et al. 2006, their Equation (2)) we integrate the modified blackbody from 8 to 1100 μm to estimate the total infrared luminosity of the continuum. We calculate a value of $L_{\rm TIR} \approx 1.0 \times 10^{13}\,L_\odot$ making the host galaxy of J0341+1720 a ULIRG.

In high-redshift quasars the far-infrared emission stems from dust, which is predominantly heated by stars (e.g., Leipski et al. 2014; Venemans et al. 2017a). Under this assumption we convert the TIR luminosity into a star formation rate of SFR $\approx 1500\,M_\odot\,{\rm yr}^{-1}$ (Murphy et al. 2011). By assuming that all dust emission is attributed to star formation, the derived star formation rate should be regarded as an upper limit. We caution that our data does not constrain the peak or shape of the SED and provide only a normalization of the chosen SED template. Thus our assumptions introduce large uncertainties of up to a factor of ∼3, as discussed in detail in Venemans et al. (2018, their Section 4.1).

4. Discussion

4.1. Lensing

Strong gravitational lensing can magnify the quasar's emission, which in turn leads to overestimates on the measured luminosity, Eddington luminosity ratio, and BH mass. As both J0341+1720 and J2125−1719 are extremely bright compared to the quasar population at the same redshifts (see Figure 1), the question arises whether their emission could have been amplified by a foreground galaxy (or galaxy cluster).

Figure 6 displays $10'' \times 10''$ cutout images of J0341+1720 and J2125−1719 from PS1 and the Vista Hemisphere Survey (VHS; McMahon et al. 2013), where available. We measured the seeing by fitting a 2D Gaussian to the quasar and adjacent stars in a $400 \times 400\,''^2$ field of view. Our results are displayed in Table 4 and show that both sources do not deviate from point sources down to the seeing limit of the images.

A cross-match between the CASTLES catalog of lensed quasars and the Gaia DR2 source catalog (Gaia Collaboration et al. 2016, 2018) showed that Gaia can detect quasar pairs and quadruples down to a separation of $0\farcs5$. A match of J0341+1720 to Gaia DR2 finds that it is the only source listed within $20''$ of its position. In the case of J2125−1719 a faint ($G = 20.96$) second source is detected within $20''$ at a separation of $6\farcs43$. This separation would be too large to

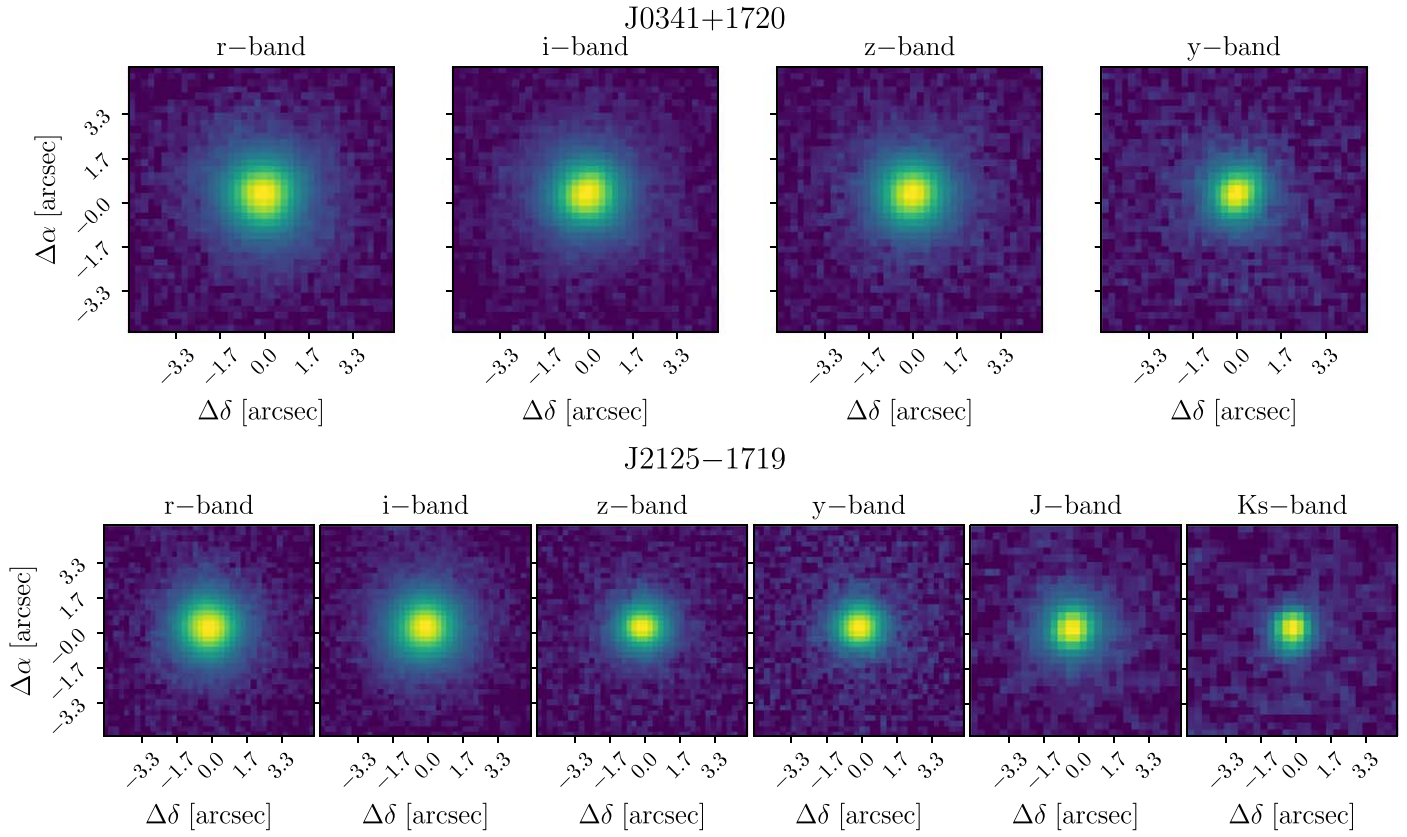

Figure 6. $10'' \times 10''$ cutout images of PS1 (r, i, z, y) photometry for J0341+1720 and J2125−1719 centered on the quasar position. We further included the VHS J- and Ks-band for J2125−1719. Both quasars are well detected in all bands, showing a point-source-like PSF with no indication for multiple images or distortions as would be expected for strongly lensed systems.

Table 4
Seeing Measurements (FWHM of a 2D Gaussian) for PS1 and VHS Photometry

Photometric Band	J0341+1720 FWHM (arcsec)	Point Sources FWHM (arcsec)	J2125−1719 FWHM (arcsec)	Point Sources FWHM (arcsec)
r-band	1.08	1.07 ± 0.06	1.27	1.23 ± 0.05
i-band	0.96	0.97 ± 0.05	1.13	1.15 ± 0.04
z-band	1.00	0.99 ± 0.04	1.02	1.03 ± 0.06
y-band	0.88	0.90 ± 0.03	1.13	1.10 ± 0.02
J-band	⋯	⋯	0.95	0.96 ± 0.03
K-band	⋯	⋯	0.83	0.82 ± 0.03

allow for substantial magnification of the quasar light. However, using Gaia we would not be able to identify lensed quasars with small image separations, such as J043947.08 +163415.7 at $z = 6.51$ (Fan et al. 2019) with an image separation of $\theta \sim 0\farcs2$.

Both photometry and Gaia cross-matches suggest that neither J0341+1720 or J2125−1719 are being strongly lensed on scales of $\gtrsim 1\farcs0$. Only high-resolution imaging using the Hubble Space Telescope or the Atacama Large Millimeter/submillimeter Array will be able to constrain lensing on smaller scales. For the remainder of this paper, we will assume these quasars not to be lensed.

4.2. Black Hole Masses and Super-Eddington Accretion

Figure 7 shows the bolometric luminosities and black hole masses of J0341+1720 (orange) and J2125−1719 (green) in comparison with other measurements from the literature. The population of low-redshift SDSS quasars ($z = 1.52$–2.2) with BH mass estimates based on detection of the Mg II line is shown in gray contours (Shen et al. 2011). Additionally, we add three ultraluminous ($M_{1450} \leqslant -29$) quasars in the literature, SMSS J2157−3602 (Wolf et al. 2018; Onken et al. 2020) at $z \approx 4.7$, SDSS J0306+1853 (Wang et al. 2015) at $z \approx 5.4$, and SDSS J0100+2802 (Wu et al. 2015) at $z \approx 6.3$, and an extremely luminous, super-Eddington quasar SDSS J0131−0321 at $z = 5.18$ (Yi et al. 2014). In all cases we adopt Mg II-based BH mass measurements based on the relation of Vestergaard & Osmer (2009) for a valid comparison. In the case of SMSS J2157-3602 and SDSS J0131−0321 we recalculate their BH mass using their Mg II FWHM and L_{3000} and for SDSS J0100+2802 we use the value of Schindler et al. (2020). J0341+1720 and J2125−1719 are much more luminous compared to the population of low- and mid-redshift SDSS quasars. They harbor SMBHs with masses of $\log(M_{\rm BH}/M_{\odot}) = 9.5$–$10$ at the massive end of the low-redshift SDSS quasar distribution. While both quasars are similarly luminous to their three ultraluminous siblings, they have lower BH masses, resulting in accretion rates moderately above the Eddington limit with $\lambda_{\rm Edd} = 2$–3. The BH mass estimates from the Hβ and Mg II lines are generally regarded as robust. Do our measurements then provide tangible evidence of super-Eddington growth in these two systems?

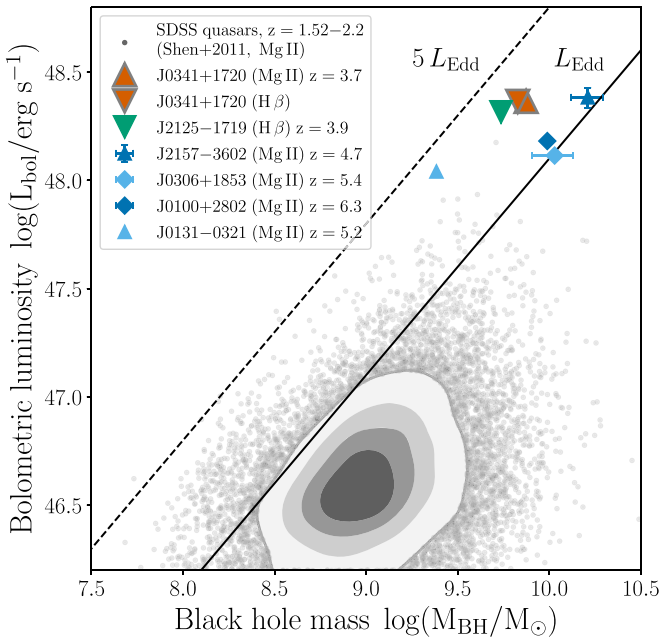

Figure 7. Bolometric luminosity as a function of black hole mass. We display the Mg II and Hβ measurements of J0341+1720 and the Hβ BH mass measurement for J2125−1719. We compare them with the individual measurements for J2157-3602 (Onken et al. 2020), SDSS J0131−0321 (Yi et al. 2014), SDSS J0306+1853 (Wang et al. 2015), and SDSS J0100+2802 (as updated in Schindler et al. 2020). The symbols for each object are illustrated in the legend. We display the distribution of low-redshift (z = 1.52–2.2) BH mass measurements of the SDSS quasar sample (Shen et al. 2011) with filled gray contours. We denote which emission line the BH mass estimate was based on in the legend and for consistency use the same single-epoch virial mass estimator for the same line. Where error bars are included, they show the statistical uncertainties of the measurements, while systematic uncertainties on the SMBH mass can be as large as 0.55 dex (Vestergaard & Osmer 2009).

In order to quantify some of the systematics associated with adopting a single-epoch virial estimator we adopt additional relations for the Hβ and Mg II lines to calculate the black hole masses. In the case of J0341+1720 we find the BH masses range between $M_{\rm BH} = (6.73–15.55) \times 10^9\,M_\odot$ based on both the Hβ and Mg II using four different single-epoch virial mass estimators (McLure & Dunlop 2002; Vestergaard & Peterson 2006; Vestergaard & Osmer 2009; Shen et al. 2011), resulting in Eddington luminosity ratios of $\lambda_{\rm Edd} = 1.18–2.74$. For J2125−1719 we find BH masses of $M_{\rm BH} = (4.53–7.53) \times 10^9\,M_\odot$ based on the Hβ and C IV line using three different single-epoch virial mass estimators (McLure & Dunlop 2002; Vestergaard & Peterson 2006), resulting in Eddington luminosity ratios of $\lambda_{\rm Edd} = 2.18–3.62$. Once we take the systematic uncertainty on the BH mass estimates of 0.55 dex into account and consider the range of BH masses derived above, J0341+1720 and J2125−1719 could have accretion rates consistent with the Eddington limit. In turn, they would also have BH masses on the order of $10^{10}\,M_\odot$.

4.3. Black Hole Galaxy Coevolution

Well established correlations between the masses of SMBHs and their host galaxy's bulge mass (e.g., Magorrian et al. 1998; Marconi & Hunt 2003; Häring & Rix 2004; Kormendy & Ho 2013) suggest a coordinated coevolution by a common physical mechanism (e.g., see Silk & Rees 1998; Di Matteo et al. 2005; Hopkins et al. 2006; Peng 2007; Jahnke & Macciò 2011; Anglés-Alcázar et al. 2013). Active galactic nuclei and quasars have been used to investigate this correlation up to $z \sim 7$ (e.g., Walter et al. 2004; Wang et al. 2010; Targett et al. 2012; Willott et al. 2015; Venemans et al. 2016; Izumi et al. 2019; Nguyen et al. 2020). In these cases the dynamical mass estimates from millimeter observations (see Section 3) have been used as an upper-limit proxy for the galaxy bulge mass.

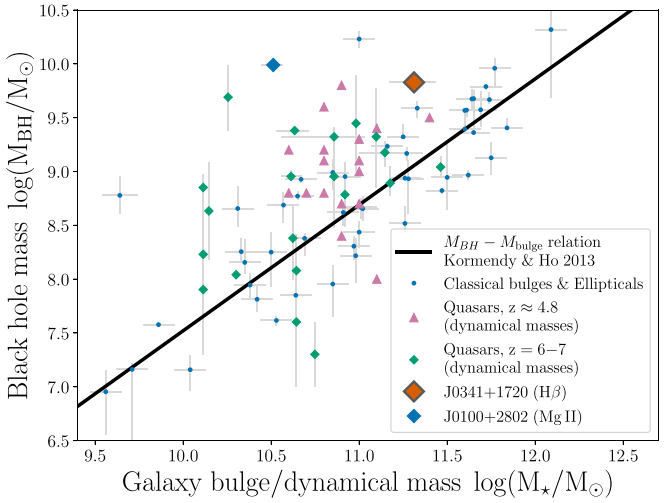

Figure 8. Black hole masses as a function of host galaxy masses. The orange diamond shows the measurement of the BH mass and galaxy host's dynamical mass (rotationally supported) for J0341+1720. We include SDSS J0100+2802 as the blue diamond (Wang et al. 2019). Purple triangles (Nguyen et al. 2020) and green diamonds (De Rosa et al. 2014; Willott et al. 2015; Venemans et al. 2016, 2017a, 2017b; Bañados et al. 2018; Izumi et al. 2019; Onoue et al. 2019) show measurements from high-redshift quasar samples. Bulge mass measurements from local galaxies (blue dots) are taken from Kormendy & Ho (2013). Similar to $z \gtrsim 4.8$ quasars J0341+1720 lies offset above from the local relation.

In Figure 8 we put our measurements of the BH mass and the host galaxy dynamical (rotationally supported) mass of J0341+1720 in context with measurements in the literature. The local black hole mass galaxy bulge mass relation is shown in black along with individual measurements from classical bulges and elliptical galaxies (blue dots; Kormendy & Ho 2013). With purple triangles and green diamonds we further display measurements from quasars at $z = 4.8$ (Nguyen et al. 2020) and at $z = 6–7$ (De Rosa et al. 2014; Willott et al. 2015; Venemans et al. 2016, 2017a, 2017b; Bañados et al. 2018; Izumi et al. 2019; Onoue et al. 2019), respectively. The majority of $z \approx 6–7$ redshift quasars are found above the local relation with the exception of a few low-luminosity high-redshift quasars (Izumi et al. 2019; Onoue et al. 2019), which scatter below. SDSS J0100+2802 (Wang et al. 2019, blue diamond) is a prominent example of an ultraluminous, high-redshift quasar lying well above the local relation. J0341+1720 is highlighted with an orange diamond above the local relation. Based on our dynamical mass estimate (rotationally supported) the host galaxy is only ∼30 times more massive than the quasar. Assuming that the quasar and the galaxy will grow continuously over the next 10 Myr, we find that this system is moving even further away from the local relation. However, we need to stress that our dynamical mass estimate is based on unresolved millimeter observations and several assumptions were made in the calculation (see Section 3). For better constraints on the host galaxy properties resolved data will be necessary.

5. Summary

In this work we have taken a closer look at two ultraluminous quasars, J0341+1720 and J2125−1719. Analysis of their full rest-frame UV to optical spectra revealed SMBHs with masses of $M_{\rm BH} = 6.73 \times 10^9\,M_\odot$ and $M_{\rm BH} = 5.45 \times 10^9\,M_\odot$, resulting in Eddington luminosity ratios of $\lambda_{\rm Edd} = 2.74$ and $\lambda_{\rm Edd} = 3.01$. Their SMBHs are among the most massive compared to black holes known (see Figure 7) and are rapidly accreting new material, possibly beyond the Eddington limit. We further observed the host galaxy emission of J0341+1720 at millimeter wavelengths with a clear detection of the CO(4–3) transition and the underlying continuum. We estimate dispersion dominated and rotationally supported dynamical masses of $M_{\rm dyn,disp} \approx 3 \times 10^{10}\,M_\odot$ and $M_{\rm dyn,rot} \approx 2 \times 10^{11}\,M_\odot$, respectively. Similarly to quasars at $z = 5$–7, J0341+1720 lies above the local SMBH galaxy scaling relations (see Figure 8). Based on its total infrared luminosity ($L_{\rm TIR} \approx 1.0 \times 10^{13}\,L_\odot$) the host galaxy of J0341+1720 can be classified as a ULIRG with an approximate star formation rate of SFR $\approx 1500\,M_\odot\,{\rm yr}^{-1}$. Given these estimates the system would evolve even further away from the local relation.

The rapid assembly of billion solar mass SMBHs in the early universe (Bañados et al. 2018; Onoue et al. 2020; Yang et al. 2020) poses challenges to standard scenarios of SMBH formation and evolution. Bounded by the Eddington limit, they could not grown to their current masses in the time since the Big Bang unless their seed masses were very high ($M_{\rm seed} > 10^4 M_\odot$). The presented analysis, highlighting two systems with evidence for super-Eddington accretion, can help to resolve some of this tension. In their recent review, Inayoshi et al. (2020) point out that the time-averaged mass accretion rate in the most massive and highest-redshift SMBHs only needs to be moderately above the Eddington limit to explain their observed masses within most BH seeding models. However, it remains an open question how such high accretion rates can be sustained, considering that the host galaxy of J0341+1720 is only ∼30 more massive than its SMBH. Only resolved millimeter observations will be able to unveil the mass, dynamics, and extent of the large gas reservoir fueling the quasars' emission.

M.N., B.V., and F.W. acknowledge support from the ERC Advanced grant 740246 (Cosmic Gas).

F.W. thanks the support provided by NASA through the NASA Hubble Fellowship grant #HST-HF2-51448.001-A awarded by the Space Telescope Science Institute, which is operated by the Association of Universities for Research in Astronomy, Incorporated, under NASA contract NAS5-26555.

This work is based on observations carried out under project number S19CZ with the IRAM NOEMA Interferometer [30 m telescope]. IRAM is supported by INSU/CNRS (France), MPG (Germany) and IGN (Spain). The authors would like to thank Jan-Martin Winters for his support with the calibration and analysis of the interferometric data.

Based on observations with the VATT: the Alice P. Lennon Telescope and the Thomas J. Bannan Astrophysics Facility.

Based on observations obtained as part of the VISTA Hemisphere Survey, ESO Progam, 179.A-2010 (PI: McMahon).

Funding for the Sloan Digital Sky Survey IV has been provided by the Alfred P. Sloan Foundation, the U.S. Department of Energy Office of Science, and the Participating Institutions. SDSS-IV acknowledges support and resources from the Center for High-Performance Computing at the University of Utah. The SDSS website is www.sdss.org. SDSS-IV is managed by the Astrophysical Research Consortium for the Participating Institutions of the SDSS Collaboration including the Brazilian Participation Group, the Carnegie Institution for Science, Carnegie Mellon University, the Chilean Participation Group, the French Participation Group, Harvard-Smithsonian Center for Astrophysics, Instituto de Astrofísica de Canarias, The Johns Hopkins University, Kavli Institute for the Physics and Mathematics of the Universe (IPMU)/University of Tokyo, the Korean Participation Group, Lawrence Berkeley National Laboratory, Leibniz Institut für Astrophysik Potsdam (AIP), Max-Planck-Institut für Astronomie (MPIA Heidelberg), Max-Planck-Institut für Astrophysik (MPA Garching), Max-Planck-Institut für Extraterrestrische Physik (MPE), National Astronomical Observatories of China, New Mexico State University, New York University, University of Notre Dame, Observatário Nacional/MCTI, The Ohio State University, Pennsylvania State University, Shanghai Astronomical Observatory, United Kingdom Participation Group, Universidad Nacional Autónoma de México, University of Arizona, University of Colorado Boulder, University of Oxford, University of Portsmouth, University of Utah, University of Virginia, University of Washington, University of Wisconsin, Vanderbilt University, and Yale University.

This work has made use of data from the European Space Agency (ESA) mission Gaia (https://www.cosmos.esa.int/gaia), processed by the Gaia Data Processing and Analysis Consortium (DPAC, https://www.cosmos.esa.int/web/gaia/dpac/consortium). Funding for the DPAC has been provided by national institutions, in particular the institutions participating in the Gaia Multilateral Agreement.

Facilities: LBT (LUCI1, LUCI2), Magellan:Baade (FIRE), VATT (VATTSpec), SOAR (Goodman High Throughput Spectrograph), IRAM:NOEMA.

Software: Astropy (Astropy Collaboration et al. 2013, 2018), SciPy (Virtanen et al. 2020), Numpy (van der Walt et al. 2011), Pandas (pandas development team 2020; McKinney 2010), LMFIT (Newville et al. 2014), Pypeit (Prochaska et al. 2019, 2020), Extinction (Barbary 2016).

Appendix
Modeling of the Optical and Near-infrared Spectra

We have used a custom interactive fitting code based on the LMFIT python package (Newville et al. 2014) package to model the spectra of both quasars. This is a two-stage process, in which we interactively set the continuum and line emission regions, add models for the continuum and the emission lines and determine the initial best fit, which is then saved. In a second step we resample each spectrum 1000 times by randomly drawing new flux values on a pixel by pixel basis from a Gaussian distribution set by the original flux values and their uncertainties. All resampled spectra are then fit using our interactively determined best-fit as the initial guess. We build posterior distributions for all fit parameters by recording the best-fit value from each resampled spectral fit. The results presented here refer to the median of this distribution and the associated uncertainties are the 13.6 and 86.4 percentile values.

The spectral fits constructed with our interactive code consist of continuum and line models. All continuum models are

subtracted from the spectrum before the line models are fit. We will now discuss the components of our continuum model and provide general properties of the emission lines included in our fits.

A.1. The Continuum Model

We model the quasar continuum with three general components. First we approximate the nonthermal radiation from the accretion disk by a single power-law normalized at 2500 Å:

$$F_{\rm PL}(\lambda) = F_{\rm PL,0}\left(\frac{\lambda}{2500\ \text{Å}}\right)^{\alpha_\lambda}. \quad \text{(A1)}$$

Here $F_{\rm PL,0}$ is the normalization and α_λ is the slope of the power law.

In addition to the power-law, high-order Balmer lines and bound-free Balmer continuum emission give rise to a Balmer pseudo-continuum. We do not model the region, where the high-order Balmer lines merge and thus we only model the bound-free emission blueward of the Balmer break at $\lambda_{\rm BE} = 3646$ Å. The Balmer continuum models follow the description of Dietrich et al. (2003), who assumed the Balmer emission arises from gas clouds of uniform electron temperature that are partially optically thick:

$$F_{\rm BC}(\lambda) = F_{\rm BC,0}\ B_\lambda(\lambda, T_e)(1 - e^{(-\tau_{\rm BE}(\lambda/\lambda_{\rm BE})^3)}),\quad \forall\,\lambda \leqslant \lambda_{\rm BE}, \quad \text{(A2)}$$

where $B_\lambda(T_e)$ is the Planck function at the electron temperature of T_e, $\tau_{\rm BE}$ is the optical depth at the Balmer edge and $F_{\rm BC,0}$ is the normalized flux density at the Balmer break (Grandi 1982). We estimate the strength of the Balmer emission, $F_{\rm BC,0}$, from the flux density slightly redward of the Balmer break at $\lambda = 3675$ Å after subtraction of the power-law continuum (Dietrich et al. 2003). We further fix the electron temperature and the optical depth to values of $T_e = 15{,}000$ K and $\tau_{\rm BE} = 1$, common values in the literature (Dietrich et al. 2003; Kurk et al. 2007; De Rosa et al. 2011; Mazzucchelli et al. 2017; Shin et al. 2019; Onoue et al. 2020).

Many quasar spectra show a strong contribution from transitions of single and double ionized iron atoms (Fe II and Fe III), which are important to correctly model the broad Mg II line as well as the Hβ and O[III] lines.

The large number of iron transitions, especially from Fe II, lead to a multitude of emission lines, which blend into an iron pseudo-continuum. We adopt the empirical and semi-empirical iron templates, derived from the narrow-line Seyfert 1 galaxy I Zwicky 1 (Boroson & Green 1992; Vestergaard & Wilkes 2001; Tsuzuki et al. 2006) to model the iron emission for the two quasar spectra.

To accurately model the Mg II inclusion of the surrounding iron emission is crucial (2200–3500 Å). As discussed in Onoue et al. (2020) and Schindler et al. (2020) the Tsuzuki et al. (2006) template, which includes an iron contribution beneath the Mg II is preferable over the Vestergaard & Wilkes (2001) in this region when measuring the Fe II or Mg II properties. However, in order to use the black hole mass scaling relations for Mg II, which were established with FWHM measurements using the Vestergaard & Wilkes (2001) template, we fit J0341+1720 with each template.

We aim to measure the properties of the Hβ line for both quasars. Similar to Mg II this line is emitted in a region with significant Fe II contribution. We adopt the empirical iron template of Boroson & Green (1992) in this region (3700–5600 Å).

The iron templates are redshifted to the systemic redshift of the quasars. In addition, we convolve the templates with a Gaussian kernel to broaden the intrinsic width of the iron emission of I Zwicky 1, FWHM $\approx 900\ \text{km s}^{-1}$, according to the quasar's broad lines (see Boroson & Green 1992, for a discussion):

$$\sigma_{\rm conv} = \sqrt{\text{FWHM}^2_{\rm obs} - \text{FWHM}^2_{\rm I\ Zwicky\ 1}}\,/\,2\sqrt{2\ln 2}. \quad \text{(A3)}$$

We set the FWHM and the redshift of the iron template in the Mg II region to the values determined from the Mg II line, while the Hβ redshift and FWHM are applied to the iron template at 3700–5600 Å (see Tsuzuki et al. 2006; Shin et al. 2019, for a similar approach). The full continuum model, including the broadened iron template, and the emission line models are fit iteratively until the FWHM of the Mg II and Hβ line converge.

Our sources are extremely luminous quasars and we therefore do not include a contribution from the stellar component of the quasar host.

We fit these three components of our continuum model to the spectra in line-free regions. Which regions in a quasar spectrum can be considered line-free is widely discussed in the literature (e.g., Vestergaard & Peterson 2006; Decarli et al. 2010; Shen et al. 2011; Mazzucchelli et al. 2017; Shen et al. 2019). We follow Vestergaard & Peterson (2006) and Shen et al. (2011) and adopt the following regions in our continuum fit: $\lambda_{\rm rest}$ = 1265–1290 Å, 1340–1375 Å, 1425–1470 Å, 1680–1705 Å, 2200–2700 Å, 4435–4700 Å. Unfortunately, the spectral coverage makes it impossible to include regions redward of the Mg II line in the fit of J0341+1720 and redward of Hβ in both fits. We interactively adjust the continuum windows to exclude regions with absorption lines, sky-line residuals or unusually large flux errors. The specific regions included in the continuum fit are shown in Figures 2 and 3 as the light blue regions on the top of each panel.

A.2. Emission Line Models

We focus our analysis of the optical and near-infrared quasar spectra on the broad Si IV, C IV, Mg II, Hβ, and O[III] lines. Given the signal-to-noise ratio and low to medium resolution of the spectra, we do not sufficiently resolve any emission line doublets or triplets and therefore model them as single lines with rest-frame wavelengths of λ1399.8 Å for Si IV, λ1549.06 Å for C IV, λ2798.75 Å for Mg II, λ4862.68 Å for Hβ, and λ4960.30 Å/λ5008.24 Å for the two [O III] lines (see Vanden Berk et al. 2001). The lines are modeled with one or two Gaussian profiles, depending on the line shape.

The broad Si IV line blends together with the close-by semi-forbidden O IV] λ1402.06 Å transition. Given the resolution and the quality of our data we cannot disentangle the two lines and rather model their blend, Si IV+O IV] λ1399.8 Å.[7]

[7] http://classic.sdss.org/dr6/algorithms/linestable.html

ORCID iDs

Jan-Torge Schindler https://orcid.org/0000-0002-4544-8242
Xiaohui Fan https://orcid.org/0000-0003-3310-0131
Mladen Novak https://orcid.org/0000-0001-8695-825X
Bram Venemans https://orcid.org/0000-0001-9024-8322
Fabian Walter https://orcid.org/0000-0003-4793-7880
Feige Wang https://orcid.org/0000-0002-7633-431X
Jinyi Yang https://orcid.org/0000-0001-5287-4242
Minghao Yue https://orcid.org/0000-0002-5367-8021
Eduardo Bañados https://orcid.org/0000-0002-2931-7824
Yun-Hsin Huang https://orcid.org/0000-0003-4955-5632

References

Anglés-Alcázar, D., Özel, F., & Davé, R. 2013, ApJ, 770, 5
Astropy Collaboration, Price-Whelan, A. M., Sipőcz, B. M., et al. 2018, AJ, 156, 123
Astropy Collaboration, Robitaille, T. P., Tollerud, E. J., et al. 2013, A&A, 558, A33
Bañados, E., Venemans, B. P., Mazzucchelli, C., et al. 2018, Natur, 553, 473
Barbary, K. 2016, extinction v0.3.0, Zenodo, doi:10.5281/zenodo.804967
Beelen, A., Cox, P., Benford, D. J., et al. 2006, ApJ, 642, 694
Boroson, T. A., & Green, R. F. 1992, ApJS, 80, 109
Boutsia, K., Grazian, A., Calderone, G., et al. 2020, ApJS, 250, 26
Calderone, G., Boutsia, K., Cristiani, S., et al. 2019, ApJ, 887, 268
Carilli, C. L., & Walter, F. 2013, ARA&A, 51, 105
Chambers, K. C., Magnier, E. A., Metcalfe, N., et al. 2016, arXiv:1612.05560
Clough, S. A., Shephard, M. W., Mlawer, E. J., et al. 2005, JQSRT, 91, 233
Coatman, L., Hewett, P. C., Banerji, M., et al. 2017, MNRAS, 465, 2120
Coatman, L., Hewett, P. C., Banerji, M., & Richards, G. T. 2016, MNRAS, 461, 647
Davies, F. B., Hennawi, J. F., Bañados, E., et al. 2018, ApJ, 864, 143
De Rosa, G., Decarli, R., Walter, F., et al. 2011, ApJ, 739, 56
De Rosa, G., Venemans, B. P., Decarli, R., et al. 2014, ApJ, 790, 145
Decarli, R., Falomo, R., Treves, A., et al. 2010, MNRAS, 402, 2453
Decarli, R., Walter, F., Venemans, B. P., et al. 2018, ApJ, 854, 97
Denney, K. D. 2012, ApJ, 759, 44
Dietrich, M., Hamann, F., Appenzeller, I., & Vestergaard, M. 2003, ApJ, 596, 817
Di Matteo, T., Springel, V., & Hernquist, L. 2005, Natur, 433, 604
Downes, D., & Solomon, P. M. 1998, ApJ, 507, 615
Fan, X., Wang, F., Yang, J., et al. 2019, ApJL, 870, L11
Fitzpatrick, E. L., & Massa, D. 2007, ApJ, 663, 320
Flesch, E. W. 2015, PASA, 32, e010
Gaia Collaboration, Brown, A. G. A., Vallenari, A., et al. 2018, A&A, 616, A1
Gaia Collaboration, Prusti, T., de Bruijne, J. H. J., et al. 2016, A&A, 595, A1
Grandi, S. A. 1982, ApJ, 255, 25
Gullikson, K., Dodson-Robinson, S., & Kraus, A. 2014, AJ, 148, 53
Häring, N., & Rix, H.-W. 2004, ApJL, 604, L89
Hopkins, P. F., Hernquist, L., Cox, T. J., et al. 2006, ApJS, 163, 1
Horne, K. 1986, PASP, 98, 609
Inayoshi, K., & Haiman, Z. 2016, ApJ, 828, 110
Inayoshi, K., Visbal, E., & Haiman, Z. 2020, ARA&A, 58, 27
Izumi, T., Onoue, M., Matsuoka, Y., et al. 2019, PASJ, 71, 111
Jahnke, K., & Macciò, A. V. 2011, ApJ, 734, 92
Jeram, S., Gonzalez, A., Eikenberry, S., et al. 2020, ApJ, 899, 76
Kaiser, N., Aussel, H., Burke, B. E., et al. 2002, Proc. SPIE, 4836, 154
Kaiser, N., Burgett, W., Chambers, K., et al. 2010, Proc. SPIE, 7733, 77330E
King, A. 2016, MNRAS, 456, L109
Kormendy, J., & Ho, L. C. 2013, ARA&A, 51, 511
Kurk, J. D., Walter, F., Fan, X., et al. 2007, ApJ, 669, 32
Leipski, C., Meisenheimer, K., Walter, F., et al. 2014, ApJ, 785, 154
Magorrian, J., Tremaine, S., Richstone, D., et al. 1998, AJ, 115, 2285
Maiolino, R., Juarez, Y., Mujica, R., Nagar, N. M., & Oliva, E. 2003, ApJL, 596, L155
Marconi, A., & Hunt, L. K. 2003, ApJL, 589, L21
Mazzucchelli, C., Bañados, E., Venemans, B. P., et al. 2017, ApJ, 849, 91
McLure, R. J., & Dunlop, J. S. 2002, MNRAS, 331, 795
McMahon, R. G., Banerji, M., Gonzalez, E., et al. 2013, Msngr, 154, 35
Mejía-Restrepo, J. E., Trakhtenbrot, B., Lira, P., & Netzer, H. 2018, MNRAS, 478, 1929
Mejía-Restrepo, J. E., Trakhtenbrot, B., Lira, P., Netzer, H., & Capellupo, D. M. 2016, MNRAS, 460, 187
Murphy, E. J., Condon, J. J., Schinnerer, E., et al. 2011, ApJ, 737, 67
Newville, M., Stensitzki, T., Allen, D. B., & Ingargiola, A. 2014, LMFIT: Non-Linear Least-Square Minimization and Curve-Fitting for Python, 0.8.0, Zenodo, doi:10.5281/zenodo.11813
Nguyen, N. H., Lira, P., Trakhtenbrot, B., et al. 2020, ApJ, 895, 74
Novak, M., Venemans, B. P., Walter, F., et al. 2020, ApJ, 904, 131
Onken, C. A., Bian, F., Fan, X., et al. 2020, MNRAS, 496, 2309
Onken, C. A., Ferrarese, L., Merritt, D., et al. 2004, ApJ, 615, 645
Onoue, M., Bañados, E., Mazzucchelli, C., et al. 2020, ApJ, 898, 105
Onoue, M., Kashikawa, N., Matsuoka, Y., et al. 2019, ApJ, 880, 77
pandas development team, T. 2020, pandas-dev/pandas: Pandas, v1.0.5, Zenodo, doi:10.5281/zenodo.3509134
Park, D., Woo, J.-H., Denney, K. D., & Shin, J. 2013, ApJ, 770, 87
Peng, C. Y. 2007, ApJ, 671, 1098
Peterson, B. M., Ferrarese, L., Gilbert, K. M., et al. 2004, ApJ, 613, 682
Prochaska, J. X., Hennawi, J., Cooke, R., et al. 2019, pypeit/PypeIt: Releasing for DOI, 0.11.0.1, Zenodo, doi:10.5281/zenodo.3506873
Prochaska, J. X., Hennawi, J. F., Westfall, K. B., et al. 2020, arXiv:2005.06505
Prochaska, J. X., Tejos, N., Crighton, N., et al. 2016, linetools/linetools: Second major release, v0.2, Zenodo, doi:10.5281/zenodo.168270
Richards, G. T., Kruczek, N. E., Gallagher, S. C., et al. 2011, AJ, 141, 167
Runnoe, J. C., Brotherton, M. S., Shang, Z., & DiPompeo, M. A. 2013, MNRAS, 434, 848
Ryan-Weber, E. V., Pettini, M., Madau, P., & Zych, B. J. 2009, MNRAS, 395, 1476
Schindler, J.-T., Fan, X., Huang, Y.-H., et al. 2019a, ApJS, 243, 5
Schindler, J.-T., Fan, X., McGreer, I. D., et al. 2017, ApJ, 851, 13
Schindler, J.-T., Fan, X., McGreer, I. D., et al. 2019b, ApJ, 871, 258
Schindler, J.-T., Farina, E. P., Banados, E., et al. 2020, arXiv:2010.06902
Schlafly, E. F., & Finkbeiner, D. P. 2011, ApJ, 737, 103
Shen, Y. 2013, BASI, 41, 61
Shen, Y., Hall, P. B., Horne, K., et al. 2019, ApJS, 241, 34
Shen, Y., Richards, G. T., Strauss, M. A., et al. 2011, ApJS, 194, 45
Shin, J., Nagao, T., Woo, J.-H., & Le, H. A. N. 2019, ApJ, 874, 22
Silk, J., & Rees, M. J. 1998, A&A, 331, L1
Simcoe, R. A., Burgasser, A. J., Schechter, P. L., et al. 2013, PASP, 125, 270
Simcoe, R. A., Cooksey, K. L., Matejek, M., et al. 2011, ApJ, 743, 21
Simcoe, R. A., Sargent, W. L. W., & Rauch, M. 2004, ApJ, 606, 92
Targett, T. A., Dunlop, J. S., & McLure, R. J. 2012, MNRAS, 420, 3621
Tody, D. 1986, Proc. SPIE, 627, 733
Tody, D. 1993, in ASP Conf. Ser. 52, Astronomical Data Analysis Software and Systems II, ed. R. J. Hanisch, R. J. V. Brissenden, & J. Barnes (San Francisco, CA: ASP), 173
Tsuzuki, Y., Kawara, K., Yoshii, Y., et al. 2006, ApJ, 650, 57
Vanden Berk, D. E., Richards, G. T., Bauer, A., et al. 2001, AJ, 122, 549
van der Walt, S., Colbert, S. C., & Varoquaux, G. 2011, CSE, 13, 22
Venemans, B. P., Decarli, R., Walter, F., et al. 2018, ApJ, 866, 159
Venemans, B. P., Walter, F., Decarli, R., et al. 2017a, ApJL, 851, L8
Venemans, B. P., Walter, F., Decarli, R., et al. 2017b, ApJ, 845, 154
Venemans, B. P., Walter, F., Neeleman, M., et al. 2020, ApJ, 904, 130
Venemans, B. P., Walter, F., Zschaechner, L., et al. 2016, ApJ, 816, 37
Vestergaard, M., & Osmer, P. S. 2009, ApJ, 699, 800
Vestergaard, M., & Peterson, B. M. 2006, ApJ, 641, 689
Vestergaard, M., & Wilkes, B. J. 2001, ApJS, 134, 1
Virtanen, P., Gommers, R., Oliphant, T. E., et al. 2020, NatMe, 17, 261
Walter, F., Carilli, C., Bertoldi, F., et al. 2004, ApJL, 615, L17
Wang, F., Wang, R., Fan, X., et al. 2019, ApJ, 880, 2
Wang, F., Wu, X.-B., Fan, X., et al. 2015, ApJL, 807, L9
Wang, R., Carilli, C. L., Neri, R., et al. 2010, ApJ, 714, 699
Wang, R., Wagg, J., Carilli, C. L., et al. 2013, ApJ, 773, 44
McKinney, W. 2010, in Proc. IX Python in Science Conf., Data Structures for Statistical Computing in Python , ed. S. van der Walt & J. Millman (Trieste: SISSA), 56
Willott, C. J., Bergeron, J., & Omont, A. 2015, ApJ, 801, 123
Wolf, C., Bian, F., Onken, C. A., et al. 2018, PASA, 35, e024
Wolf, C., Hon, W. J., Bian, F., et al. 2020, MNRAS, 491, 1970
Wu, X.-B., Wang, F., Fan, X., et al. 2015, Natur, 518, 512
Yang, J., Wang, F., Fan, X., et al. 2020, ApJL, 897, L14
Yi, W.-M., Wang, F., Wu, X.-B., et al. 2014, ApJL, 795, L29